Acta Crystallographica Section D
Biological Crystallography
ISSN 0907-4449

Towards automated Laue data processing: application to the choice of optimal X-ray spectrum

Dominique Bourgeois,[a,b]* Ulrike Wagner[c] and Michael Wulff[a]

[a]ESRF, BP 220, 38043 Grenoble CEDEX, France, [b]LCCP, UPR 9015, IBS, 41 Avenue des Martyrs, 38027 Grenoble CEDEX 1, France, and [c]Abteilung für Strukturbiologie, Institut für Chemie, Karl-Franzens-Universität Graz, A-8010 Graz, Austria

Correspondence e-mail: bourgeoi@esrf.fr

Received 20 March 2000
Accepted 8 May 2000

Laue data reduction has now reached a level of sophistication that allows nearly automated processing to be performed. The software described enables complete reduction of the data with essentially no user intervention, making Laue processing almost as straightforward as monochromatic data processing. Interactive work is limited to the indexing of only one Laue pattern. More importantly, it is shown that the data quality is substantially enhanced when soft-limited predictions are used. Further improvement obtained by taking advantage of the structure-factor amplitudes from a known closely related structure is described. To determine the most suitable type of insertion device to be used for time-resolved Laue crystallography, the technique described was applied to Laue data sets collected from photoactive yellow protein under identical conditions but with three different insertion devices: a wiggler, a broad-bandpass undulator and a single-line undulator. Although the optimal choice may ultimately be dictated by sample parameters (such as mosaic spread) and by the type of experiment (repeatable or non-repeatable reactions), the results here show that the use of single-line undulators will generally yield by far the best compromise between data quality, acquisition time and radiation damage.

1. Introduction

The availability of third-generation synchrotron sources has triggered new interest in using the Laue technique to perform time-resolved experiments on macromolecules (Moffat, 1998; Ren *et al.*, 1999). In the last few years, the most spectacular results have concerned photosensitive systems, in which a time resolution of a few nanoseconds could be achieved (Srajer *et al.*, 1996; Perman *et al.*, 1998).

Wigglers have long been considered as the insertion devices (IDs) of choice for Laue crystallography because they provide a smooth and broad bandpass of X-rays (Helliwell *et al.*, 1989). Although it has been suggested that a bandpass of only one octave would be optimal (Sweet *et al.*, 1993), confidence in wigglers was reinforced as data-processing software allowing deconvolution of spatial and harmonic overlaps became available (Campbell & Hao, 1993; Ren & Moffat, 1995; Shrive *et al.*, 1990; Wakatsuki, 1993; Bourgeois *et al.*, 1998, Yang *et al.*, 1998, Nieh *et al.*, 1999).

However, based on the success of undulators for monochromatic data collection, including the field of MAD crystallography, Laue researchers recently started to reconsider which insertion device they should use. This question also arose as the single-pulse Laue technique (SP-Laue) was developed (Bourgeois *et al.*, 1996). In this case, the strong

polychromatic background generated by a wiggler is particularly detrimental to the inherently poor signal-to-noise ratio (S/N ratio) owing to ultrashort exposures. Furthermore, a wide bandpass is not strictly necessary when repeatable reactions are studied, as data for a single time point can be gathered from a large number of frames recorded at many crystal orientations. It was found that a special type of undulator, called a single-line undulator, is of special interest in the study of repeatable reactions by the SP-Laue technique, giving rise to the so-called 'pink' SP-Laue technique (Wulff *et al.*, 1997).

With a bandpass of a few keV and a peak-brilliance $\sim$100 times higher than that achievable with wigglers, a single-line undulator presents key advantages. (i) The X-ray background, being proportional to the bandpass, is greatly diminished. (ii) The integrated intensity of stimulated reflections is higher, owing to enhanced spectral flux in the narrow bandpass. (iii) Fewer reflections are stimulated per image, leading to a drastic reduction in the number of spatial and harmonic overlaps. (iv) The low divergence of the undulator beam improves the diffraction-spot shape, giving rise to a further increase in the S/N ratio. (v) The heat-load on the beamline optics is reduced, providing a more stable beam. (vi) The X-ray radiation damage on the sample is expected to be lower, because both the absorbed peak-power and the integrated absorbed energy (taking into account the total exposure time) are reduced. (vii) Finally, the limited power of the X-ray beam reduces the consequences of potential accidents such as a direct hit of the detector by the beam.

However, these advantages may be counterbalanced by a number of drawbacks. (i) Image indexing might be tricky as a consequence of there being fewer reflections recorded per image and the subsequent difficulty in identifying nodals and conics that are characteristic of Laue patterns, especially with crystals of small unit cell. (ii) Wavelength normalization is rendered difficult by the steep variations in the X-ray spectrum, although it was shown recently (Srajer *et al.*, 2000) that successful normalization could be achieved by using methods based on Chebyshev polynomials (Ren & Moffat, 1995; Arzt *et al.*, 1999). However, such variations might become harmful for low-resolution reflections spanning a large wavelength range. These reflections might even end up being partially recorded (Ren *et al.*, 1999). The problem will be exemplified in a time-resolved experiment, where the lack of synchronicity and/or thermal gradients may generate a transient increase of the crystal mosaicity. (iii) The data quality may be hampered by the presence of a limited flux at the residual second harmonic of the undulator, increasing the number of multiples that need deconvolution. (iv) Last but not least, the minimum number of Laue images collected at different crystal orientations that are necessary to record a complete data set is in theory significantly higher than when a broad-bandpass ID is used. This may pose a problem for repeatable reactions that are triggered by a UV/visible light pulse before every X-ray exposure. More light must be delivered to the sample per recorded reflection and optical radiation damage may occur before data collection is completed. One would also expect that because of the necessity of a large number of images, single-line undulators may not be used for studying single-turnover reactions (for such reactions, however, collecting monochromatic data from cryo-trapped intermediates is often more successful; Hajdu & Andersson, 1993). In these cases, an acceptable compromise could be obtained with a classical undulator displaying a sufficient bandpass while generating a moderate amount of background radiation. However, even for wide-bandpass IDs, and contrary to early predictions (Clifton *et al.*, 1991), the collection of only a few Laue frames is in general not sufficient to obtain complete data at low resolution, even for high-symmetry space groups. Furthermore, substantial redundancy is required to properly normalize the data and achieve an acceptable S/N ratio.

Therefore, it is of importance to decide on the most appropriate ID for conducting time-resolved Laue experiments, especially in the case of repeatable reactions studied with the SP-Laue technique. A first attempt to compare Laue data acquired on myoglobin crystals with different IDs has recently been described (Srajer *et al.*, 2000). It was shown that wiggler, undulator as well as single-line undulator data could be successfully processed using the *LAUEVIEW* package. However, data were not collected under strictly identical conditions and no firm conclusions could be drawn as to whether one ID was preferable to another. In this paper, we describe an experiment specifically designed to provide a fair comparison between the performance of the three IDs (U20 single-line undulator, U46 broad-bandpass undulator and W70 wiggler; Wulff *et al.*, 1997) installed on beamline ID09 at the ESRF. A single crystal of photoactive yellow protein (PYP) was used to collect three data sets using the three IDs. We show that the data collected with U20 are of outstanding quality and are far superior to those collected with broad-bandpass IDs. Only when the number of exposures has to be kept to a strict minimum (because of severe optical radiation damage or for some rapid single-turnover reactions) is the best compromise achieved with a U46-like undulator.

In this paper, we also detail the procedure by which Laue data can be processed in a nearly automated way. User intervention is limited to indexing a single image and determining a few parameters. The processing chain from indexing to final merging of the data is then automatically performed. This greatly facilitates and speeds up the treatment of Laue data. We also emphasize the advantages in using soft-limited predictions (SLPs) rather than hard-limited predictions (HLPs). SLPs match observed diffraction spots much more faithfully than HLPs. When sharply varying X-ray spectra from undulators are used, SLPs are essential to prevent integration of many non-measurable reflections. Such reflections, if included, are assigned integrated intensities corresponding to the shot-noise fluctuations of the X-ray background. These intensities are amplified in the normalization procedure and, although their $I/\sigma(I)$ values stay low, they contaminate the valid data to a considerable extent, sometimes to a point where the scaling algorithm starts to diverge. SLPs have been implemented in *LAUEVIEW* and the advantages of the technique have been reviewed by Ren *et al.* (1999). We describe two techniques to generate the SLPs. The

first one is called WDRL (wavelength-dependent resolution limit) and is based on the idea originally proposed by Bourenkov *et al.* (1996) and elaborated by Ren *et al.* (1999). In this technique, the resolution limit is fine-tuned across the X-ray spectrum as a function of wavelength. This greatly improves the quality of Laue data, especially when they are collected with undulators. The second technique is an extension of WDRL and is referred to as WMDP (wavelength and monochromatic dependent predictions). In a time-resolved experiment aiming at solving the structure of short-lived intermediates, a set of monochromatic structure-factor amplitudes corresponding to a closely related structure (a 'resting' or a 'dark' state) is generally available. Whereas this additional information may be incorporated in wavelength normalization (Campbell *et al.*, 1998; Arzt *et al.*, 1999), it can also be advantageously used in fine-tuning the SLPs. We demonstrate that the WMDP technique significantly enhances the ability of Laue data to detect subtle structural rearrangements.

2. Description of the experiment

The experiment was performed at the ID09 beamline of the ESRF with crystals of PYP from *Ectothiorhodospira halophila* (Borgstahl *et al.*, 1995). PYP is a photosensor that enters a photocycle upon absorption of a blue photon. This allows the bacterium to detect and swim away from too high levels of blue light. The radiation stiffness of PYP crystals and their high-symmetry space group ($P6_3$) make them excellent for time-resolved Laue studies. Early intermediates in the protein photocycle were identified at room temperature with m.s. and n.s. Laue crystallography (Genick *et al.*, 1997; Perman *et al.*, 1998).

A single PYP crystal ($440 \times 100 \times 100$ µm) mounted in a capillary on a single-axis diffractometer at ambient temperature was used for all data collections. Data were collected in an interleaved way: at each angular setting of the crystal, three Laue patterns were recorded successively with U20, U46 and W70. This was to eliminate the bias that would result from the gradual onset of radiation damage or from beamline instabilities. The angular settings of the crystal followed a 'gap-filling' algorithm: the total angular range was partitioned into two equal segments and diffraction patterns were first collected at the beginning of these segments. Each segment was then sub-partitioned into two half sub-segments. Data were collected at the beginning of these sub-segments and the procedure was iterated until the chosen angular step was reached. This algorithm ensures a homogeneous sampling of reciprocal space even if radiation damage develops or data collection has to be stopped. In this way, the data obtained with the three IDs were strictly comparable. The crystal started to degrade shortly after the three data collections had been completed.

The ESRF storage ring was operated in the 2/3 filling mode at ~200 mA. The gaps of the IDs were set to 16.3 mm for U20 and 25 mm for both U46 and W70. Data were recorded on a 130 mm diameter X-ray image intensifier coupled to a CCD camera (XRII/CCD) developed at the ESRF (Moy, 1994). Spatial and flat field distortions were corrected on line with a routine similar to the one implemented in *FIT2D* (Hammersley *et al.*, 1994). All experimental conditions were kept identical for the three IDs. The exposure time was 40 µs. Although one might argue that optimal experimental settings are dependent on the X-ray spectrum used, we chose this approach to avoid considering too many parameters having interrelated and poorly controlled effects. The main parameter that should be adjusted is the crystal-to-detector distance since (i) the separation between adjacent spots depends on the ID and (ii) diffraction spots of high S/N ratio are found at larger Bragg angles with U20 than with W70. However, it was too impractical to translate the detector at every exposure and it was judged more important to average out potential radiation damage by using the interleaved acquisition procedure described above. The detector distance was set to 140 mm, which gave the best compromise between spot separation with W70 and sufficiently large cutoff Bragg angle for U20.

The spacing between successive spindle angles, $\Delta\varphi$, for the three IDs were chosen in order to achieve comparable completeness of the data according to the formula

$$\Delta\varphi = \sin^{-1}(\lambda_{\max}/2d) - \sin^{-1}(\lambda_{\min}/2d),$$

where $\lambda_{\max}$ and $\lambda_{\min}$ are the maximum and minimum wavelengths and d is the resolution. Estimation of $\lambda_{\max}$ and $\lambda_{\min}$ is generally difficult and is quite meaningless for undulators with several harmonics. Aiming at complete (low-resolution) data at 8 Å and taking values of 0.32 and 0.7 Å for $\lambda_{\min}$ and 1.28 and 0.95 Å for $\lambda_{\max}$ for W70 and U20, respectively, we chose angular steps of 3° for W70 and 1° for U20. U46 was set in between with angular steps of 2°, with the same $\lambda_{\max}$ and $\lambda_{\min}$ as W70. The total angular range was 90°, allowing complete coverage of the reciprocal space whatever the initial orientation of the crystal.

3. Data processing

3.1. Data sets from U20, U46 and W70

Data sets from all three IDs were processed in essentially the same way and to the same resolution limit of 1.9 Å. Only the wavelength limits $\lambda_{\max}$ and $\lambda_{\min}$ as well as the order of Chebyshev polynomials for wavelength normalization were chosen differently (50, 60 and 20 for U20, U46 and W70, respectively; these values gave the best compromise between scaling performance, computation time and appearance of spurious oscillations in the normalization curves). For each ID, SLPs were generated with both the WDRL and WMDP techniques. Monochromatic structure-factor amplitudes $F_{\rm mono}$s used in WMDP were derived from a previous experiment on similar PYP crystals. Thus, six data sets were obtained that are referred to as u20, u46, w70 and $u20_{\rm mono}$, $u46_{\rm mono}$, $w70_{\rm mono}$ (in the following, lower-case 'u' refer to data sets and upper-case 'U' to IDs). For the U20 data, two additional processing sessions were performed: one with a wide wave-

length range (referred to as $u20_{large}$, λ_{min} = 0.35 Å, λ_{max} = 1.2 Å), which includes the contribution of the residual second harmonic, and one which only includes frames collected at the same spindle orientations as used for W70, referred to as $u20_{w70}$. In a similar way, an additional set was processed for U46, referred to as $u46_{w70}$.

3.2. Automated Laue data processing

Laue data sets can be processed automatically once a single image has been interactively indexed. Fig. 1 shows a flow chart of the successive steps performed in a processing session. A single command file launches the whole session. The set of software includes *LAUEGEN* (indexing, positional refinement, generation of HLPs; Campbell *et al.*, 1998), *PrOW* (generation of SLPs, integration; Bourgeois *et al.*, 1998), *LSCALE* (extraction of normalization curve, absorption correction, data scaling; Arzt *et al.*, 1999), *SCALA* (data merging; Collaborative Computational Project, Number 4, 1994) and finally *TRUNCATE* (computation of structure-factor amplitudes from intensities; French & Wilson, 1978).

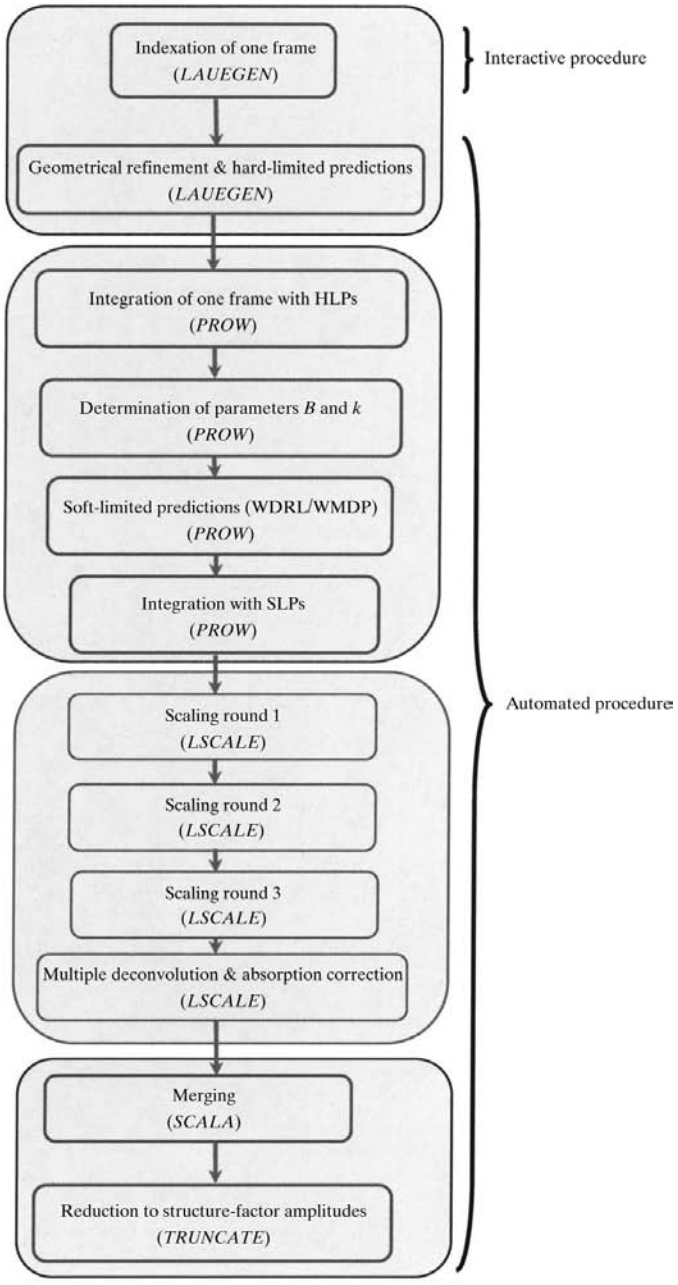

Figure 1
Flow chart of Laue data processing.

3.2.1. *LAUEGEN*. A routine written in c-shell language has been set up which makes use of *LAUEGEN* to determine the orientation matrices of a series of Laue patterns, refine them and generate HLPs for each of them. The correct orientation matrix as well as the hard limits d_{min}, λ_{min} and λ_{max} for one of the patterns must have been determined interactively in a previous stage using the *LAUEGEN* graphical user interface. This is the only manual intervention required during the whole processing of the data set. It is acceptable to slightly overestimate the hard limits, since WDRL/WMDP filtering in *PrOW* will remove most of the unobservable reflections at the next stage. For each pattern, refinement of the orientation matrix proceeds from the knowledge of the matrix of the previous frame. Detector distortion parameters (twist, tilt and bulge), detector distance and possibly unit-cell parameters are also refined, but in contrast to the orientation matrix the starting values for each frame are set to nominal values in order to avoid potential drifts. Positional refinement is performed with reflections of sufficient *S*/*N* ratio, predicted within restricted resolution and wavelength ranges (d_{min} = 2.5 Å, λ_{min} = 0.4 Å and λ_{max} = 1.2 Å for W70 and U46 data).

3.2.2. *PrOW*. Integration of Laue patterns can either be performed with HLPs (as output by *LAUEGEN*) or with SLPs. Recent developments for the generation of SLPs with either WDRL or WMDP are described in §3.3.

Integration of Laue patterns is performed as described in Bourgeois *et al.* (1998). The ability of *PrOW* to determine an optimal fitting area $\mathcal{R}$ independently for each reflection improves the accuracy of the integration of weak diffraction spots. The areas $\mathcal{R}$ are also used to automatically flag spatially overlapped spots, so that deconvolution is only performed when appropriate (Bourgeois, 1999).

3.2.3. *LSCALE*. Wavelength normalization and data scaling are performed with the program *LSCALE* (Arzt *et al.*, 1999), in three rounds. In the first round, data to a reduced resolution limit are used and a first set of scale factors, *B* factors and Chebyshev polynomials are calculated. Since these factors may be influenced by outliers, the latter, as determined from the first round, are removed in the second round from the input data and a second set of scale factors, *B* factors and Chebyshev polynomials are derived. Finally, using this second set as starting values and all data (initial outliers may turn out not to be outliers), a third final set of scale factors, *B* factors and Chebyshev polynomials are determined. Global absorption correction and deconvolution of the multiples are also performed at this stage. All data satisfying the criterion $|I_{scaled} - I_{mean}|/I_{mean} < 0.5$ are finally output, where I_{scaled} is the scaled integrated intensity and I_{mean} is the average of I_{scaled} over symmetry-related reflections.

Table 1
Comparison of statistical factors for U20 data collected with HLPs or SLPs.

The WDRL technique was used. The fraction of reflections selected with WDRL was ∼54%.

	R_{sym}†	Completeness	Redundancy
HLPs	8.1	96.1	7.1
SLPs	6.3	98.1	8.2

† $R_{sym} = \sum_{hkl}\sum_i |I_i - \langle I\rangle| / \sum_{hkl}\sum_i |I_i|$.

3.3. Generation of SLPs

Let us consider a reflection h measured at wavelength λ. A likely calculated integrated intensity $I_{calc}(h)$ can be assigned to h as

$$I_{calc}(h) \propto I_0(\lambda) L\left[F^2_{mono}(h)\right] \exp\left(-B/2d^2\right). \quad (1)$$

$I_0(\lambda)$ is the predicted normalization curve at λ (which takes into account the incident X-ray spectrum, isotropic absorption effects, the detector response and a factor λ^2; Bourgeois *et al.*, 1996), $L = (2\sin^2\theta)^{-1}$ is the Lorentz factor (θ is the Bragg angle), $d = \lambda/2\sin\theta$ is the resolution and B is a temperature factor. Effects of polarization are neglected. The factor $F_{mono}(h)$ is the structure-factor amplitude of h measured in a previous monochromatic experiment. It is included in the WMDP technique but is ignored in WDRL. This structure-factor amplitude is generally available (unless monochromatic diffraction data were recorded from a crystal in a different space group) and typically refers to the sample in its ground state. It is expected to deviate moderately from the one measured by Laue, which refers to either ground or excited states. The WDRL/WMDP techniques reject all HLPs that do not satisfy the criterion

$$I_{calc}(h) \geq k, \quad (2)$$

where k is a cutoff threshold. An approximation of $I_0(\lambda)$ might be obtained from a previous experiment performed with the same experimental setup. The difficulty therefore consists in determining B accurately and choosing k objectively. The factor B might be extracted from a Wilson plot derived from the merged data, but this has the inconvenience that full processing with HLPs or guessed B and k parameters must be performed beforehand, which may produce inaccurate results. Furthermore, with WMDP, damping factors owing to atomic displacement parameters are already included in F_{mono}s. As isotropic B factors derived from Laue data are usually higher than those observed with monochromatic data (because of the intense background, the S/N ratio decreases faster with resolution in the Laue case), only the difference must be applied in this case. Concerning the choice of the threshold k, no method has yet been described. It is therefore desirable to determine B and k in a reliable way that is free of user bias. We propose the following method, which only necessitates the integration with HLPs of one (preferably the first) frame of the Laue data set. The result of this integration yields a set of integrated intensities $\{I_{HL}\}$. Based on the knowledge of $\{I_{HL}\}$ and of the approximated normalization curve leading to a calculated set $\{I_{calc}\}$, S/N ratio considerations and a histogram-matching technique are used to optimally choose B and k. Details of the procedure can be obtained from bourgeoi@esrf.fr.

Using only one Laue image to determine B and k is not optimal if the crystal quality decays significantly during data

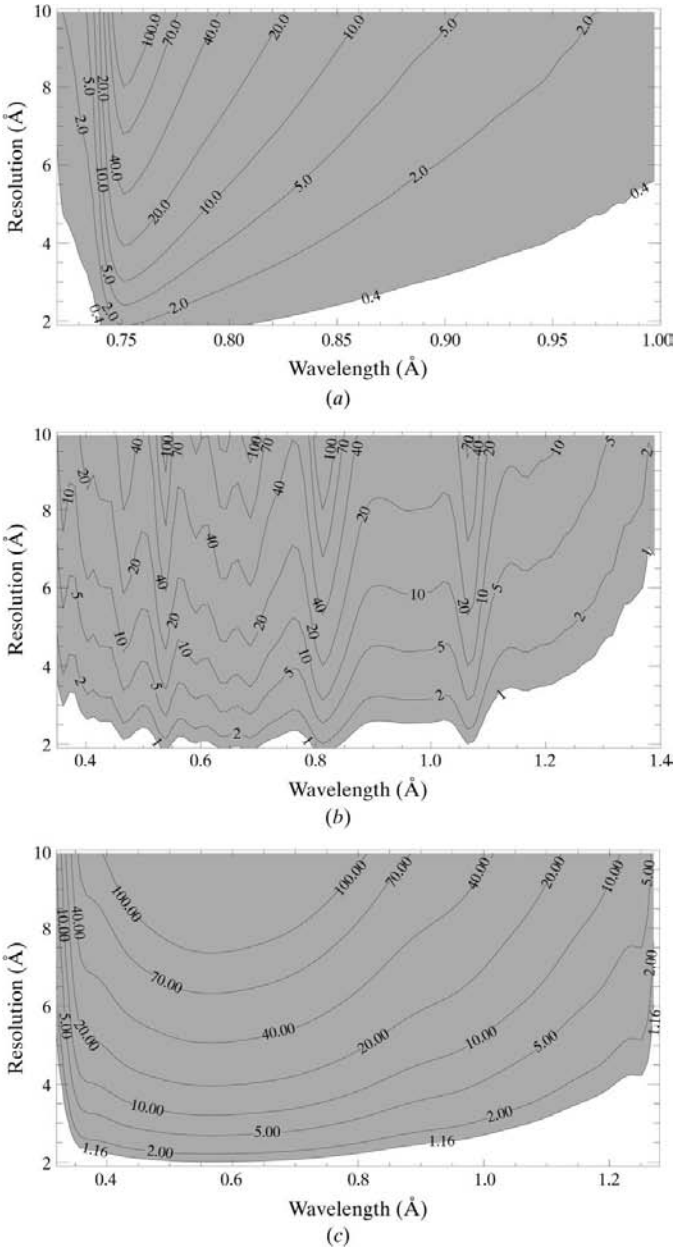

Figure 2
Plots of resolution ranges selected by the WDRL technique as a function of wavelength for (*a*) U20, (*b*) U46 and (*c*) W70. Contour levels correspond to predicted intensities I_{calc} expressed as percentage of a reference intensity taken at 8 Å at the peak of the normalization curve. The last contour line corresponds to the cutoff level k [see (2)]. (k, B) values are (0.4, 5.43), (1.0, 13.97) and (1.16, 19.21) for U20, U46 and W70, respectively. For U20, the B value of 5.43 is probably underestimated as a result of the Bragg angle cutoff arising from the limited size of the detector. When WMDP is used, (k, B) changes to (0.46, 2.24), (3.48, 5.11) and (3.39, 5.63), respectively.

collection. In such a case, using the first image of the set leads to some over-prediction of the SLPs. This is usually acceptable, but the data set can alternatively be split into a number of subsets for which independent *B*s and *k*s are determined.

4. Results and discussion

4.1. Soft-limited predictions, normalization curves

Although data sets from the three IDs could be processed successfully with HLPs instead of SLPs, the results were significantly worse. An example is shown for the U20 data in Table 1. The improvement obtained with WDRL/WMDP is outstanding. Although many more diffraction spots are integrated when HLPs are used, fewer successful measurements are output by *LSCALE* than when SLPs are used. This is related to the great difficulty in scaling the former data correctly. Attempts to process $u20_{large}$ with HLPs completely failed owing to divergence of the normalization procedure.

The WDRL technique allows assessment of the effective resolution limit as a function of wavelength, as shown in Fig. 2. It is clearly seen that U20 data reach a resolution higher than the used hard-limit of 1.9 Å: the last contour line is severely truncated at wavelengths located at the top of the U20 fundamental. We estimate that data from U20 could have been processed to better than 1.8 Å. However, the Bragg angle cutoff imposed by the limited size of the detector prevented this. In contrast, the resolution limit achieved with W70 data is lower than 1.9 Å. A satisfactory match is obtained for U46, which suggests that in terms of the high-resolution limit U46 should be preferred to W70.

The efficiency of the WDRL/WMDP techniques in filtering out non-measurable reflections is shown in the histograms of Fig. 3. The vast majority of the weak reflections are properly filtered out. However, a limited number of high I/σ_I reflections are rejected with WDRL, whereas this number becomes insignificant with WMDP. In both cases, a small amount of low I/σ_I measurements are not rejected, re-emphasizing the fact

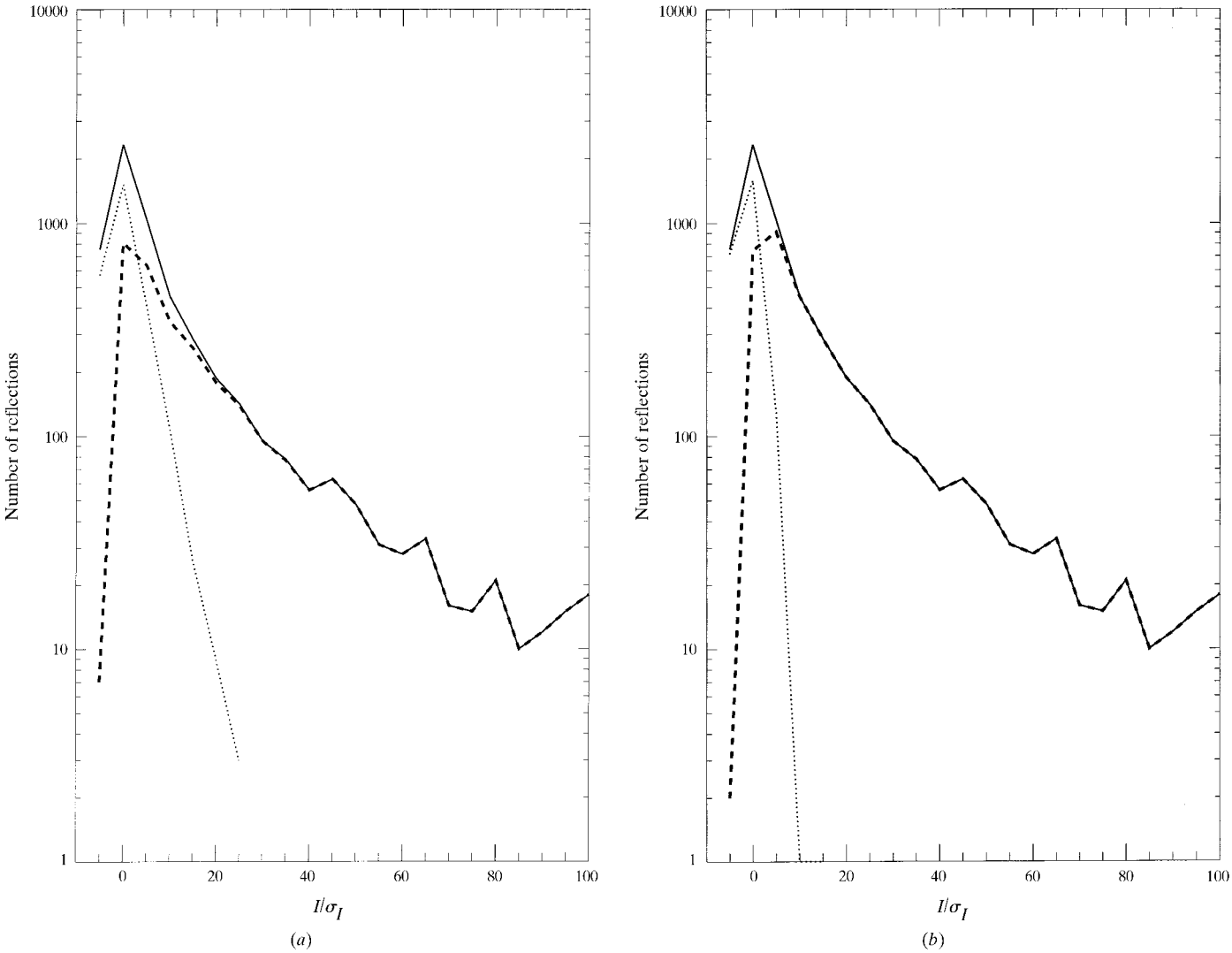

Figure 3
Histograms of I/σ_I calculated from the set $\{I_{HL}\}$ with U46. The solid-line histogram corresponds to all HLPs in $\{I_{HL}\}$, the dashed-line histogram to SLPs and the dotted-line histogram to the filtered-out predictions. (*a*) WDRL technique; (*b*) WMDP technique.

that the WDRL/WMDP techniques perform a more subtle treatment of the data than simply applying a I/σ_I cutoff.

The quality of the integration by *PrOW* and especially the deconvolution of spatial overlaps is demonstrated by looking at the correlation between the integrated intensities of the reflections selected by WDRL when the latter technique is applied before or after integration (not shown). This correlation is virtually perfect (>0.999 for w70), with only very few reflections deviating significantly between the two experiments.

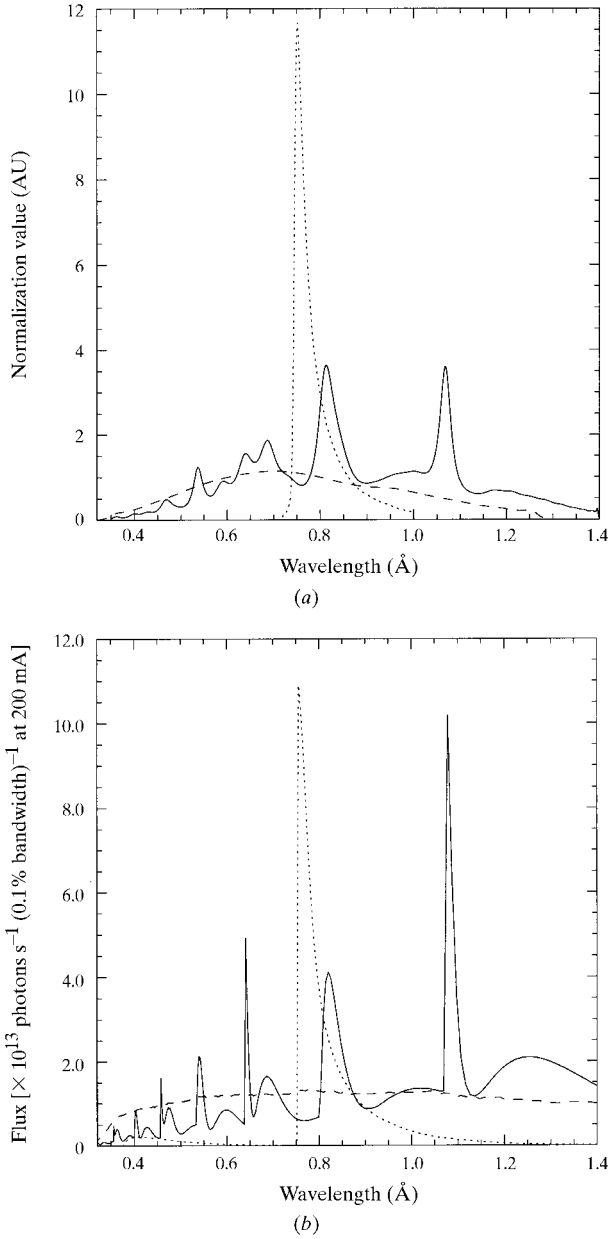

Figure 4
(*a*) Final normalization curves from U20 (dotted-line), U46 (solid-line) and W70 (dashed-line) as output by *LSCALE* (round 3). These curves were obtained when the WMDP technique was used. (*b*) Calculated X-ray spectra from U20 (dotted-line), U46 (solid-line) and W70 (dashed-line). In these spectra, the electron energy dispersion, the filters inserted in the beamline (0.5 mm of carbon, two beryllium windows, air path), the mirror reflectivity, the absorption profile of the detector and the scattering efficiency were not taken into account. This explains the discrepancies observed between (*a*) and (*b*). AU, arbitrary units.

Table 2
Number of measurements rejected in u20, u46, w70, $u20_{mono}$, $u46_{mono}$ and $w70_{mono}$.

	Number of predictions	Rejections by *PrOW*	Rejections by *LSCALE*	Rejections by *SCALA*	Global fraction rejected (%)
u20	86790	18	11693	2073	15.9
u46	120510	14	26829	2302	24.2
w70	91815	73	23562	1812	27.7
$u20_{mono}$	92001	11	6187	1846	8.7
$u46_{mono}$	125094	18	15384	1836	13.8
$w70_{mono}$	98947	74	17293	1693	19.3

Final normalization curves produced by *LSCALE* are shown in Fig. 4(*a*). Most features in these curves can clearly be correlated to variations observed in the calculated X-ray spectra from the three IDs (Fig. 4*b*). The first eight harmonics of U46 can easily be recognized in the corresponding normalization curve. The shoulder at 0.94 Å in the W70 curve is assigned to the L_{III} absorption edge of platinum, the coating material of the focusing mirror of the beamline. In the U46 normalization curve, signs of spurious wiggles appear at the edges of the wavelength range, showing that the number of Chebyshev coefficients should not be increased further.

Rejection statistics for the six data sets u20, $u20_{mono}$, u46, $u46_{mono}$, w70 and $w70_{mono}$ are shown in Table 2. A marginally small number of reflections are rejected by *PrOW*, corresponding to spots being assigned a non-realistic negative value or having a faulty background. The small number of measurements rejected by *SCALA* proves the efficiency of the normalization and rejection criterion applied by *LSCALE*. When WMDP is used, the number of outliers diminishes greatly, despite increased multiplicity. This is ascribed to the higher quality of the predictions. However, it is important to realise that in all cases a significant fraction of the measurements are rejected at the normalization stage. This has been observed for the vast majority of Laue structures published so far. Histograms of the rejected measurements as a function of wavelength, as shown in Fig. 5, clearly reveal that outliers are concentrated where the X-ray flux is low. Most outliers originate from weak measurements for which statistical errors are amplified through the large scaling factor applied to them. There are only few outliers at wavelengths where the derivative of the normalization curve is high, showing the high accuracy of the latter.

4.2. Data quality, correlation with monochromatic data

Detailed statistics for u20, u46 and w70 are shown in Fig. 6 and global statistics for all data sets are summarized in Table 3. The u20 data are by far superior to the u46 and w70 data: they are nearly complete, with a *S*/*N* ratio well above those of u46 and w70 as a result of the lower X-ray background. Although at medium resolution the multiplicity is lower, the pooled coefficient of variation (PCV; Diederichs & Karplus, 1997), which represents a combined figure of merit between R_{sym} and

Table 3
Comparison of statistical factors for u20, u46, w70, $u20_{mono}$, $u46_{mono}$, $w70_{mono}$, $u20_{w70}$ and $u46_{w70}$.

The values are given for the whole resolution range (30–1.9 Å). Numbers were obtained from *SCALA* output files.

	R_{sym}† (%)	R_{meas0}‡ (%)	PCV0§ (%)	I/σ_I	Completeness (%)	Redundancy
u20	6.3	6.7	9.0	8.2	98.1	8.7
u46	9.1	9.5	15.0	6.4	90.4	11.9
w70	9.4	9.9	14.0	6.6	75.4	10.3
$u20_{mono}$	8.4	8.7	11.4	6.6	93.8	10.5
$u46_{mono}$	10.8	11.1	15.6	5.8	75.8	16.9
$w70_{mono}$	11.1	11.5	15.0	5.8	70.7	13.3
$u20_{w70}$	5.8	6.6	8.5	9.1	95.5	4.0
$u46_{w70}$	9.0	9.5	14.5	6.7	89.3	9.0

† $R_{sym} = \sum_{hkl}\sum_i|I_i - \langle I\rangle|/\sum_{hkl}\sum_i|I_i|$. ‡ R_{meas0}, multiplicity-weighted R_{sym} (relative to the overall mean). See Diederichs & Karplus (1997). § PCV0: pooled coefficient of variation (relative to the overall mean). See Diederichs & Karplus (1997).

redundancy, remains better. It also appears that the dependence of the u20 data quality on resolution is flatter than that observed for u46 and w70. This is because more low-resolution reflections are measured with a weak *S*/*N* ratio at wavelengths remote from the U20 fundamental and more high-resolution reflections are measured with a high *S*/*N* ratio at wavelengths close to the fundamental.

At very low resolution, a significant degradation of the u20 data is observed. Normalization errors arise from the fact that, depending on crystal mosaicity, low-resolution reflections span a significant wavelength range. This results in scaling difficulties when variations in the X-ray spectrum are sharp. It also produces partially recorded reflections because of the narrow bandpass of U20 (Ren *et al.*, 1999). These effects may generate problems in a time-resolved experiment, where poor synchronicity in conformational changes and/or thermal gradients may produce a transient increase in crystal mosaicity. However, they could be counterbalanced by applying to the reflections a weighted average of the scale factors corresponding to their wavelength span, instead of the scale factor corresponding to their central wavelength, as is presently performed. A small improvement may also be expected from tapering U20 in order to slightly increase the bandpass and produce a smoother spectrum. A similar behaviour is observed with the u46 data, although to a lesser extent.

The results obtained for u46 and w70 are globally quite comparable, although the w70 data are slightly less complete at low resolution and significantly less complete at high resolution (in accordance with Fig. 3). The w70 data show a slightly more satisfactory *S*/*N* ratio, especially at low resolution, but they are less redundant.

When only singles are included in the processing, the completeness in the lowest resolution bin is decreased by only 0.36% for u20, by 14.4% for u46 and by 17.3% for w70. This shows that deconvolution of multiples is almost unnecessary with U20, but is mandatory for U46 and W70.

The excellent quality of the $u20_{w70}$ data set is striking. The completeness of these data is only slightly reduced at low resolution relative to u20 and remains much higher than the

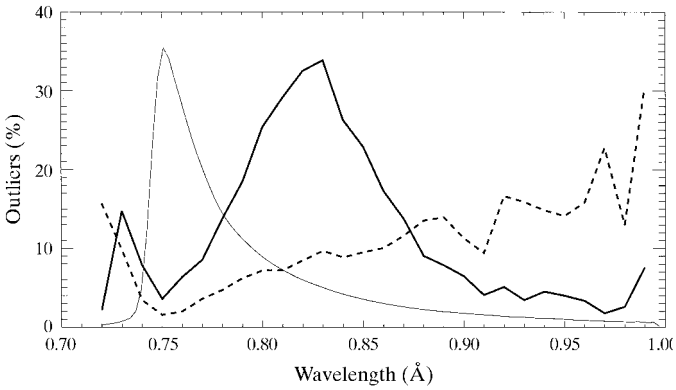

Figure 5
Fraction of measurements rejected by *LSCALE* (round 3) as a function of wavelength in the case of U20. The thin line is the U20 normalization curve. The solid-line histogram was obtained with WDRL and the dashed-line histogram with WMDP. In the latter case, outliers are distributed differently and tend to concentrate in regions of very small X-ray flux, where reflections with large F_{mono}s are still predicted.

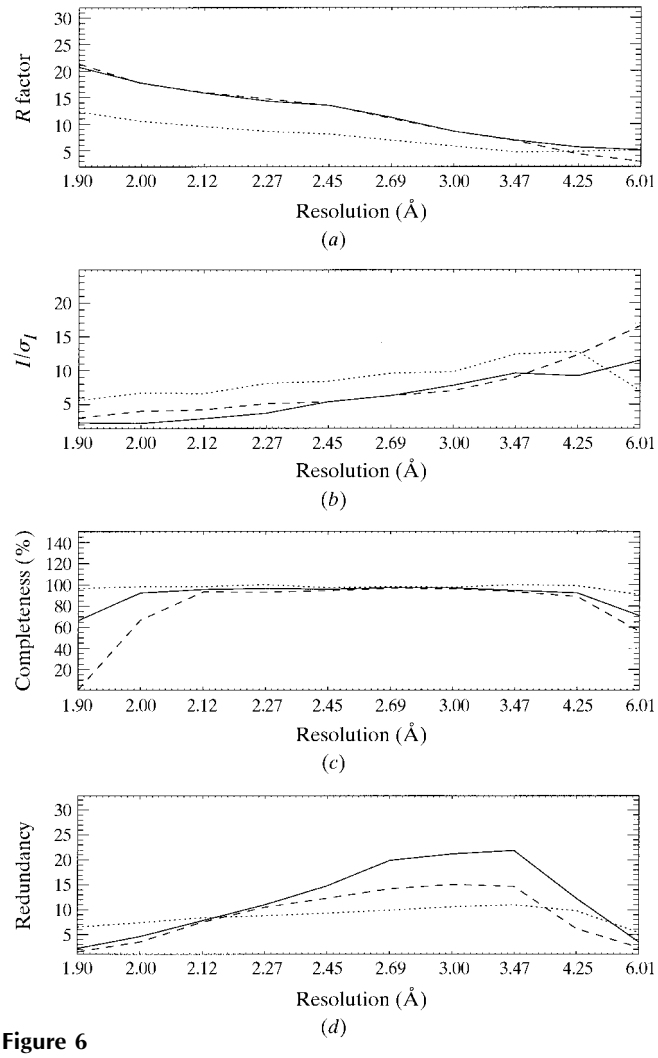

Figure 6
Statistical results obtained with data sets u20 (dotted line), u46 (plain line) and w70 (dashed line). (*a*) *R* factor, (*b*) I/σ_I, (*c*) completeness, (*d*), redundancy.

completeness of w70. The same observation is made for $u46_{w70}$ relative to u46. It appears that the necessity of a small angular step in collecting Laue data with U20 or U46 is not as strict as anticipated. This is an important finding in terms of light-induced radiation damage in time-resolved experiments (and in terms of total duration of the data collection). The minimal number of spindle orientations could possibly be reduced further if – as is usually performed with monochromatic data – a test exposure is performed initially in order to determine the crystal orientation and to plan an optimal strategy for data collection. In fact, it turned out that our PYP crystal was initially oriented with its c^* axis almost parallel to the spindle axis. A proper total angular range of 30° should therefore have been sufficient to collect nearly complete data. Processing of the corresponding subsets of $u20_{w70}$ and w70 (*i.e.* with only the first ten images included) surprisingly showed that a better completeness was still achieved with U20 [76.3% overall completeness (52.7% in the lowest resolution bin) for the subset of $u20_{w70}$ compared with 65.8% (34.8%) for the subset of w70, although at medium resolution the latter subset was superior]. It is expected that large-bandpass IDs are preferable only when very few Laue frames are to be recorded (as for rapid single-turnover reactions). In such a case, U46 should be chosen instead of W70.

The absorbed X-ray dose was estimated to be 0.5 mJ for $u20_{w70}$, 3.4 mJ for $u46_{w70}$ and 3.9 mJ for w70. Therefore, the X-ray-induced radiation damage is strongly reduced when U20 is used, whereas optical damage would be identical for the three data sets. It is striking to observe that a typical monochromatic data collection with U20 would lead to an absorbed dose of ~0.6 mJ, very similar to the value obtained in polychromatic mode. However, secondary radiation damage is expected to be much more severe in the Laue case.

When the second harmonic of the U20 spectrum is taken into account, a serious degradation of the data quality is observed: $u20_{large}$ is much worse than u20. The normalization curve at the peak of the second harmonic is only 0.6% of the

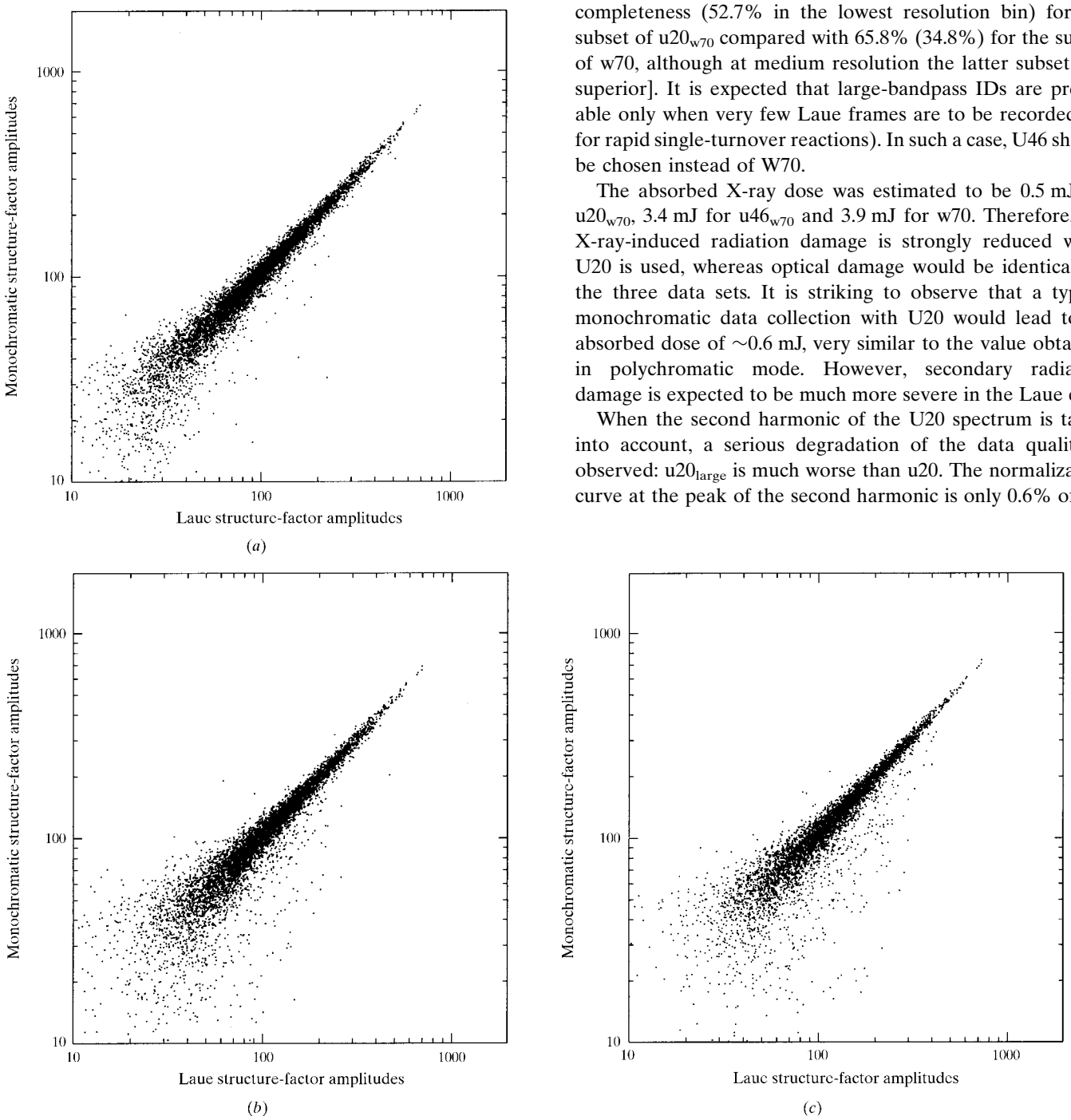

Figure 7
Correlation plots between Laue and monochromatic structure-factor amplitudes for (*a*) U20, (*b*) U46 and (*c*) W70. The correlations are 0.989 for U20, 0.975 for U46 and 0.966 for W70. These plots were obtained with WDRL. With WMDP, the correlation factors increase to 0.989 for $u20_{mono}$, 0.981 for $u46_{mono}$ and 0.974 for $w70_{mono}$. The corresponding plots are slightly more tight than those shown.

Table 4
Refinement statistics for $mono_{1.9}$, u20, u46, w70, $u20_{mono}$, $u46_{mono}$, $w70_{mono}$, $u20_{w70}$ and $u46_{w70}$.

Initial R_{cryst} factors were around 26% for all data sets.

	R_{cryst} (%)	R_{free} (%)	σ_A†	RMS back‡	RMS side§	Real-space R¶	$\langle B\rangle$††	Tot_{H_2O}‡‡	OK_{H_2O}§§
$mono_{1.9}$	18.59	22.45	0.05	0.099	0.211	5.43	12.83	48	30
u20	19.25	24.0	0.08	0.115	0.234	6.63	15.0	47	30
u46	20.07	24.36	0.17	0.122	0.240	9.44	14.78	49	27
w70	20.09	26.41	0.20	0.135	0.264	12.80	13.61	46	25
$u20_{mono}$	18.82	23.00	0.06	0.117	0.231	6.70	14.95	49	29
$u46_{mono}$	18.02	23.5	0.08	0.119	0.245	9.27	15.07	42	24
$w70_{mono}$	18.68	25.23	0.06	0.138	0.267	11.55	14.22	41	20
$u20_{w70}$	19.54	23.9	0.08	0.114	0.235	7.76	14.76	41	27
$u46_{w70}$	20.46	24.91	0.18	0.127	0.249	10.52	14.27	42	27

† σ_A coordinate error. ‡ Average RMS backbone deviation (Å). The RMS deviation is defined as $\left[\left(\sum_{i=1}^{N} d_i^2\right)/N\right]^{1/2}$, where d_i is the distance between the positions of the same atom i in two different models, $i = 1 \ldots N$ and N is the number of atoms in the backbone or the side chain of the residue under study. RMS deviations from ideal geometry average to 0.0055 Å for bond lengths and to 1.240° for bond angles, with non-significant deviations between data sets. § Average RMS side-chain deviation (Å). ¶ Real-space R factor (in %) between σ_A-weighted ($2F_{Laue} - F_{calc}$) and calculated F_{calc} maps. †† Average atomic displacement factor. ‡‡ Total number of water molecules. §§ Number of water molecules matching water molecules of the target model (*i.e.* distant by less than 0.5 Å).

fundamental. Therefore, the contribution of the data recorded close to the second harmonic is small relative to the errors made by using a unique (or even two separate, not shown) wavelength range(s) that include(s) both harmonics. It is therefore a better choice to leave out the second harmonic.

Correlation plots between Laue structure-factor amplitudes and their (target) monochromatic counterparts are shown in Fig. 7. These plots are of excellent quality, although a very slight systematic error is observed with all three IDs: Laue structure-factor amplitudes tend to be slightly overestimated relative to the monochromatic ones. This might be a result of multiples being treated as singles and is more pronounced for W70 and U46 than for U20. In contrast, few strong (low-resolution) reflections are less well measured with U20 than with W70, in agreement with the less satisfactory statistics of the former ID in the lower resolution bins.

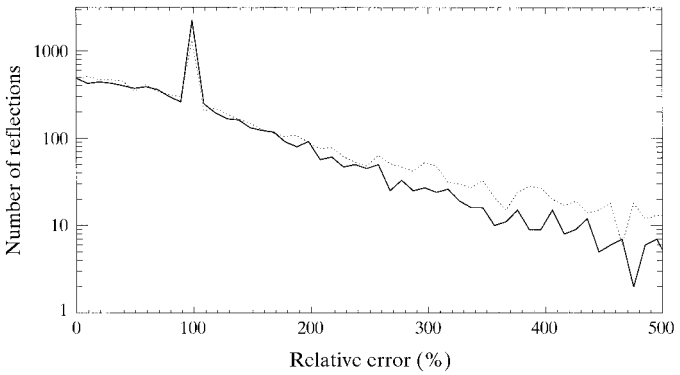

Figure 8
Histograms of errors ε made in Laue structure-factor amplitudes, relative to an assumed ΔF set to 10% of F_{mono}, corresponding to some structural changes, in the case of U46. For measured data, the error in F_{Laue} is assumed to be $|F_{Laue} - F_{mono}|$. For unmeasured data, the error is equal to ΔF, *i.e.* the relative error is 100%. The solid-line histogram was obtained with WMDP and the dotted-line histogram was obtained with WDRL. The height of the spike at 100% relative error reflects the incompleteness of the data. With WMDP the incompleteness increases, but the additional missing data are essentially those that were located on the right side of the spike in the dotted curve, *i.e.* those that have a relative error of more than 100% when WDRL is used.

4.3. The WMDP technique

The trends described in §4.2 are also observed for the $u20_{mono}$, $u46_{mono}$ and $w70_{mono}$ data sets. However, the S/N ratios are worse, the completeness appears to be reduced and redundancies increase. These features are explained by the fact that both the WDRL and WMDP techniques select approximately the same number of predictions. However, the distribution of the SLPs is different in each case. With WMDP, reflections with weak monochromatic structure-factor amplitudes tend to be left out, whereas reflections with strong monochromatic structure-factor amplitudes are measured with a higher redundancy at wavelengths corresponding on average to weaker regions of the X-ray spectrum. Scaling of the data is therefore more affected by large variations in the X-ray spectrum, which explains the observed degradation in the S/N ratio and why it is more pronounced for U20 (19.5%) than for W70 (12%). The degradation also results from the greatly reduced number of outliers (see Table 2) contributing to the extra redundancy. The completeness of the data is only lower because the reflections that are left out are those whose structure-factor amplitudes are effectively very close to zero. The decrease is much smaller for U20 than for U46 and W70 because weak data can be measured more reliably with the former ID.

Removal of weakly diffracting reflections as performed by WMDP is only justified if the errors made in measuring their structure-factor amplitudes F_{Laue} are greater than the errors made by replacing the left-out F_{Laue}s by their F_{mono} counterparts in subsequent structural refinement. The histogram in Fig. 8 shows, taking the case of U46, that this is likely to be the case when small structural changes are expected. To compute this histogram, we imagine that our Laue data set was collected in order to detect structural modifications and that these modifications can be expressed by a change in structure-factor amplitude ΔF equal to 10% of F_{mono}. We then assume that for measured reflections the error ε made in F_{Laue} is expressed by $|F_{Laue} - F_{mono}|$ (that is, F_{mono} is a target value) and that for unmeasured reflections the error is simply ΔF. When WMDP is used, it appears that a drastic reduction in the average fractional error $\varepsilon/\Delta F$ is obtained compared with when WDRL is used. This result is true for all three IDs. The reduction reaches 22% for $u20_{mono}$ relative to u20, 39% for $u46_{mono}$ relative to u46 and 41% for $w70_{mono}$ relative to w70. Average absolute errors $\langle\varepsilon\rangle$s follow the same trend. The

improvement is larger when the data quality is lower and it can be seen again that data from U20 surpasses data from the two other IDs. If ΔF is taken to be 20% of $F_{\rm mono}$, a large reduction in $\varepsilon/\Delta F$ is still observed with WMDP. However, if ΔF is taken to be 100% of $F_{\rm mono}$ (the case of normal refinement as opposed to difference refinement), we observe increases of 7.6, 26.8 and 18.9%, respectively, in the fractional error when WMDP is used instead of WDRL. From these results, we expect that using WMDP instead of WDRL for generating the SLPs should bring improvement when computing omit maps from PYP (see below). Most importantly, significant improvements would be expected in the refinement of small structural changes but not in the refinement of a native structure.

4.4. Chromophore omit maps

The u20, u46, w70, u20$_{\rm mono}$, u46$_{\rm mono}$ and w70$_{\rm mono}$ data sets were used to calculate difference omit maps using phases from the 1.4 Å model of Borgstahl *et al.* (1995), in which the 4-hydroxy-cinnamoic cofactor was removed (as well as a sphere of 1.5 Å around it). As a comparison, a subset of the 1.4 Å monochromatic data (Borgstahl *et al.*, 1995) extending to 1.9 Å (referred to as mono$_{1.9}$) was used to compute a 'target' omit map. To avoid phase memory bias, the procedure described by Hodel *et al.* (1992) was applied. Results are shown in Fig. 9. Three observations can be made. Firstly, the quality of the two maps calculated from U20 data is outstanding and approaches that of the map obtained with mono$_{1.9}$. Secondly, there is degradation in going from U20 to U46 and W70. Thirdly, the use of WMDP brings significant improvement for all three IDs. The improvement is more pronounced for W70 and U46, emphasizing that the WMDP technique is of special importance when broad-bandpass IDs are used. The difference between the omit maps obtained with w70 and w70$_{\rm mono}$ shows that the lower quality of the W70 maps relative to the U20 maps is not only a consequence of the lower completeness, but also of the lower *S*/*N* ratio.

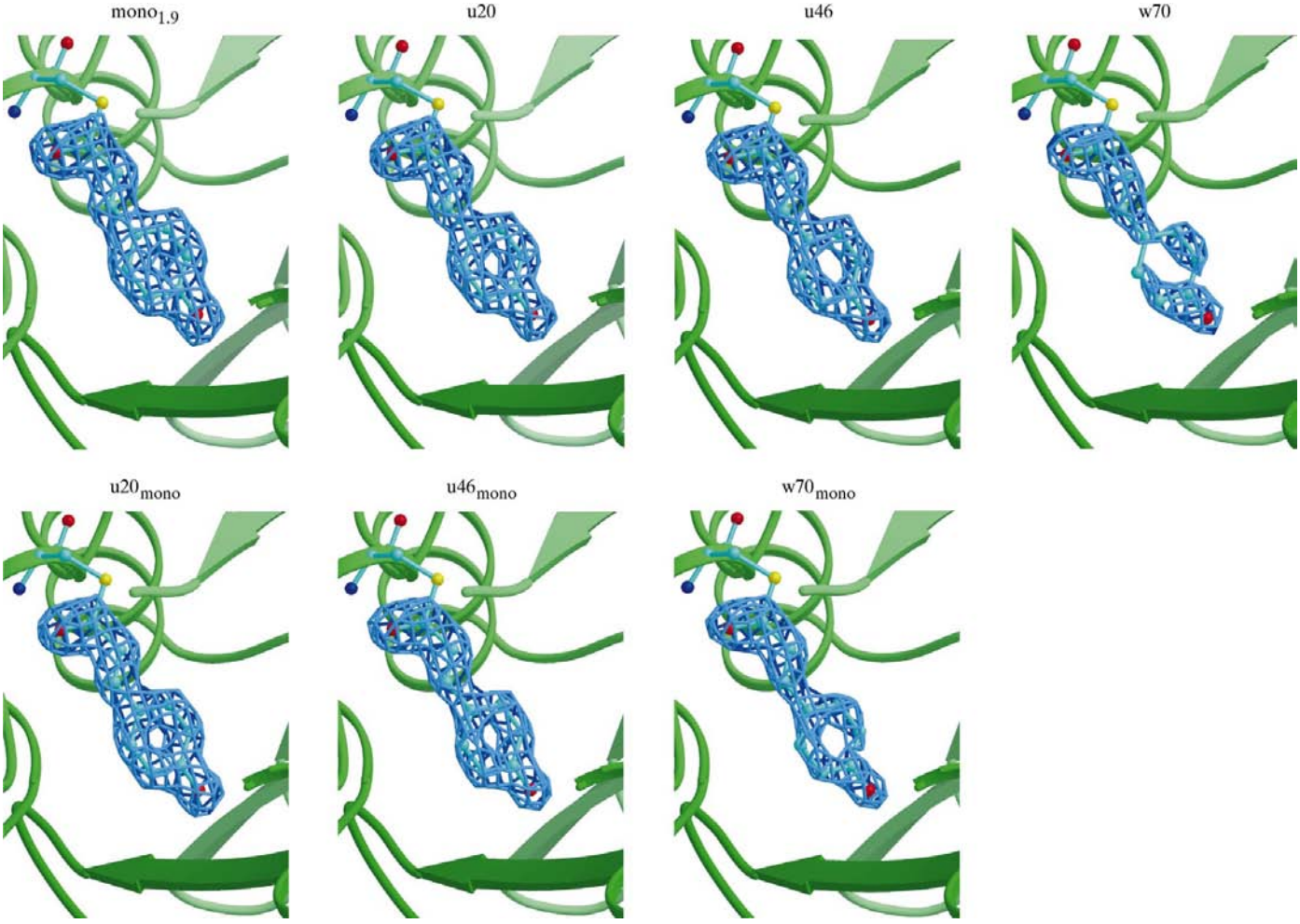

Figure 9
Difference omit maps calculated with the mono$_{1.9}$, u20, u46, w70, u20$_{\rm mono}$, u46$_{\rm mono}$ and w70$_{\rm mono}$ data sets. Maps are displayed at a contour level of 4.5σ. Discontinuity appear at levels of 7.4σ for mono$_{1.9}$, 6.1σ for u20, 5.0σ for u46, 4.2σ for w70, 6.5σ for u20$_{\rm mono}$, 5.5σ for u46$_{\rm mono}$, 4.6σ for w70$_{\rm mono}$ (5.1σ for u46$_{\rm w70}$ and 6.0σ for u20$_{\rm w70}$). This clearly shows the superior quality of the data from U20. It also emphasizes the importance of using WMDP rather than WDRL. The quality of omit maps calculated with u46$_{\rm w70}$ and u20$_{\rm w70}$ (not shown) closely approaches that obtained with u46 and u20. The figure was prepared with *BOBSCRIPT* (Esnouf, 1997).

4.5. Structure refinement

Models of PYP were refined against the $mono_{1.9}$, u20, u46, w70, $u20_{mono}$, $u46_{mono}$, $w70_{mono}$, $u46_{w70}$ and $u20_{w70}$ data sets using *CNS* (Brunger *et al.*, 1998). A starting model was derived from the 1.4 Å structure of PYP (Borgstahl *et al.*, 1995): all water molecules were removed and the model was 'heated' to 2000 K for 50 steps in order to generate some noise. In the following, the original 1.4 Å structure of PYP is referred to as the 'target' model. For all data sets, the same 5% of the reflections were used for cross-validation (Brünger, 1992). The refinement procedure consisted in (i) initial rigid-body refinement, (ii) a fivefold cycle of conjugate-gradient minimization, individual *B*-factor refinement and automatic water picking and deleting and (iii) a final positional and *B*-factor refinement. This procedure was applied in a strictly identical manner for all data sets. There was no manual user intervention in order to eliminate potential bias from one structure to another. However, this resulted in slightly less than optimal models. Refinement statistics are reported in Table 4. Refinements from all data sets were successful, with the expected superior quality of models derived from U20 data relative to models derived from U46 and W70 data. Three figures of merit were considered: (i) the root-mean-square (RMS) backbone and side-chain deviations from the target model; (ii) the real-space *R* factor between calculated and experimental maps and (iii) the number of water molecules successfully retrieved from those of the target model. These figures of merit (see Table 4) confirm our expectations from §4.2: the quality of data from U20 approaches that of monochromatic data, whereas data from W70 show the largest deviation. The ability to faithfully recover the water molecules is satisfactory in all cases, although data from U20 are slightly better performing. Most water molecules with *B* factors lower than $\sim$30 Å^2 in the target model are well retrieved, whereas more loosely defined water molecules in that model are less well recognized.

As predicted in §4.3 and although the R_{cryst} and R_{free} factors are slightly better, there is no marked improvement when WMDP is used instead of WDRL. However, the refinement of a native structure that we have made is not usually carried out with Laue data (if that were the case, F_{mono}s would not be available!). Rather, Laue data sets are expected to reveal small conformational changes of a well known structure and this is why we suggest using WMDP whenever possible. Atomic models of transient states should then be refined against data of the type $F_{mono} + \Delta F_{Laue}$ (with $\Delta F_{Laue} = 0$ for the rejected reflections; Terwilliger & Berendzen, 1995, 1996). Further improvement can be obtained by making use of the *Q*-weighting technique (Ursby & Bourgeois, 1997).

5. Conclusions

Several conclusions can be drawn from this work. (i) Laue data can now be processed successfully in a nearly automated way. (ii) The determination of soft-limited predictions is of primary importance to optimize data quality. This is especially true when data are collected from undulators. (iii) The use of monochromatic structure-factor amplitudes from a closely related structure in soft-limited predictions, by allowing elimination of low *S*/*N* reflections that may eventually diminish the information content of the data, brings substantial improvements when subtle structural differences are expected. (iv) Of the three insertion devices tested, a single-line undulator such as U20 gives by far the best results when a sufficient number of images can be collected: the *S*/*N* ratio of the data is higher, scaling can be successfully performed, X-ray-induced radiation damage is lower and nearly full completeness can be achieved with fewer spindle orientations than anticipated. A similar completeness is extremely difficult to obtain with wide-bandpass insertion devices, owing to the intense background and the presence of high-order multiples. (v) However, when undulators are used, low X-ray flux at some wavelengths (between the harmonics) introduce statistical noise that decreases the *S*/*N* ratio of low-resolution data. At low resolution partiality effects are also present, which may degrade time-resolved data when transient mosaic spread is observed. Improvements in the processing of Laue data can be envisaged to correct for partiality and reduce these problems. Although a firm conclusion will necessitate the study of real-time-resolved data, we recommend the use of a single-line undulator when repeatable reactions are studied with the SP-Laue technique. Even slow non-repeatable processes could be followed successfully with such an insertion device. For faster single-turnover reactions, the best compromise appears to be a relatively large bandpass undulator such as U46. A wiggler of the type W70 is not the most appropriate choice for Laue data collection.

We thank U. Genick and E. Getzoff for supplying the PYP crystals, and F. Schotte and S. Techert for assistance during the experiment. We thank S. Arzt for assistance with *LSCALE*. We acknowledge S. Wakatsuki and T. Ursby for careful reading of the manuscript.

References

Arzt, S., Campbell, J. W., Harding, M. M., Hao, Q. & Helliwell, J. R. (1999). *J. Appl. Cryst.* **32**, 554–562.
Borgstahl, G. E. O., Williams, D. R. & Getzoff, E. D. (1995). *Biochemistry*, **34**, 6278–6287.
Bourenkov, G. P., Popov, A. N. & Bartunik, H. D. (1996). *Acta Cryst.* A**52**, 797–811.
Bourgeois, D. (1999). *Acta Cryst.* D**55**, 1733–1741.
Bourgeois, D., Nurizzo, D., Kahn, R. & Cambillau, C. (1998). *J. Appl. Cryst.* **31**, 22–35.
Bourgeois, D., Ursby, T., Wulff, M., Pradervand, C., LeGrand, A., Schildkamp, W., Labouré, S., Srajer, V., Teng, T. Y., Roth, M. & Moffat, K. (1996). *J. Synchrotron Rad.* **3**, 65–74.
Brünger, A. T. (1992). *Nature (London)*, **355**, 472–474.
Brunger, A. T., Adams, P. D., Clore, G. M., DeLano, W. L., Gros, P., Grosse-Kunstleve, R. W., Jiang, J. S., Kuszewski, J., Nilges, M., Pannu, N. S., Read, R. J., Rice, L. M., Simonson, T. & Warren, G. L. (1998). *Acta Cryst.* D**54**, 905–921.
Campbell, J. W. & Hao, Q. (1993). *Acta Cryst.* A**49**, 889–893.

Campbell, J. W., Hao, Q., Harding, M. M., Nguti, N. D. & Wilkinson, C. (1998). *J. Appl. Cryst.* **31**, 496–502.
Clifton, I. J., Elder, M. & Hajdu, J. (1991). *J. Appl. Cryst.* **24**, 267–277.
Collaborative Computational Project, Number 4 (1994). *Acta Cryst.* D**50**, 760–763.
Diederichs, K. & Karplus, P. A. (1997). *Nature Struct. Biol.* **4**, 269–275.
Esnouf, R. M. (1997). *J. Mol. Graph.* **15**, 132–134.
French, S. & Wilson, K. (1978). *Acta Cryst.* A**34**, 517–525.
Genick, U. K., Borgstahl, G. E. O., Ng, K., Ren, Z., Pradervand, C., Burke, P. M., Srajer, V., Teng, T. Y., Schildkamp, W., McRee, D. E., Moffat, K. & Getzoff, E. D. (1997). *Science*, **275**, 1471–1475.
Hajdu, J. & Andersson, I. (1993). *Annu. Rev. Biophys. Biomol.* **22**, 467–498.
Hammersley, A. P., Svensson, S. O. & Thompson, A. (1994). *Nucl. Instrum. Methods A*, **346**, 312–321.
Helliwell, J. R., Habash, J., Cruickshank, D. W. J., Harding, M. M., Greenhough, T. J., Campbell, J. W., Clifton, I. J., Elder, M., Machin, P. A., Papiz, M. Z. & Zurek, S. (1989). *J. Appl. Cryst.* **22**, 483–497.
Hodel, A., Kim, S.-H. & Brünger, A. T. (1992). *Acta Cryst.* A**48**, 851–858.
Moffat, K. (1998). *Acta Cryst.* A**54**, 833–841.
Moy, J. P. (1994). *Nucl. Instrum. Methods A*, **348**, 641–644.
Nieh, Y. P., Raftery, J., Weisgerber, S., Habash, J., Schotte, F., Ursby, T., Wulff, M., Hädener, A., Campbell, J. W., Hao, Q. & Helliwell, J. R. (1999). *J. Synchrotron Rad.* **6**, 995–1006.
Perman, B., Srajer, V., Ren, Z., Teng, T. Y., Pradervand, C., Ursby, T., Bourgeois, D., Schotte, F., Wulff, M., Kort, R., Hellingwerf, K. & Moffat, K. (1998). *Science*, **279**, 1946–1950.
Ren, Z., Bourgeois, D., Helliwell, J. R., Moffat, K., Srajer, V. & Stoddard, B. L. (1999). *J. Synchrotron Rad.* **6**, 891–917.
Ren, Z. & Moffat, K. (1995). *J. Appl. Cryst.* **28**, 461–468.
Shrive, A., Clifton, I. J., Hajdu, J. & Greenhough, T. J. (1990). *J. Appl. Cryst.* **23**, 169–174.
Srajer, V., Crosson, S., Schmidt, M., Key, J., Schotte, F., Anderson, S., Perman, B., Ren, Z., Teng, T. Y., Bourgeois, D., Wulff, M. & Moffat, K. (2000). *J. Synchrotron Rad.* **7**, 236–244.
Srajer, V., Teng, T. Y., Ursby, T., Pradervand, C., Ren, Z., Adachi, S., Schildkamp, W., Bourgeois, D., Wulff, M. & Moffat, K. (1996). *Science*, **274**, 1726–1729.
Sweet, R. M., Singer, P. T. & Smalås, A. (1993). *Acta Cryst.* D**49**, 305–307.
Terwilliger, T. C. & Berendzen, J. (1995). *Acta Cryst.* D**51**, 609–618.
Terwilliger, T. C. & Berendzen, J. (1996). *Acta Cryst.* D**52**, 743–748.
Ursby, T. & Bourgeois, D. (1997). *Acta Cryst.* A**53**, 564–575.
Wakatsuki, S. (1993). *Proceedings of the CCP4 Study Weekend. Data Collection and Processing*, edited by L. Sawyer, N. W. Isaacs & S. Bailey, pp. 71–79. Warrington: Daresbury Laboratory.
Wulff, M., Schotte, F., Naylor, G., Bourgeois, D., Moffat, K. & Mourou, G. (1997). *Nucl. Instrum. Methods A*, **398**, 69–84.
Yang, X., Ren, Z. & Moffat, K. (1998). *Acta Cryst.* D**54**, 367–377.